

NOPE-SAC: Neural One-Plane RANSAC for Sparse-View Planar 3D Reconstruction

Bin Tan, Nan Xue, Tianfu Wu, Gui-Song Xia

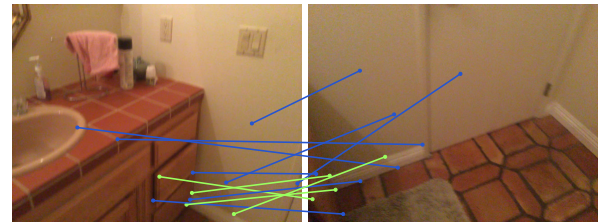
Abstract—This paper studies the challenging two-view 3D reconstruction in a rigorous sparse-view configuration, which is suffering from insufficient correspondences in the input image pairs for camera pose estimation. We present a novel *Neural One-Plane RANSAC framework* (termed NOPE-SAC in short) that exerts excellent capability to learn one-plane pose hypotheses from 3D plane correspondences. Building on the top of a siamese plane detection network, our NOPE-SAC first generates putative plane correspondences with a coarse initial pose. It then feeds the learned 3D plane parameters of correspondences into shared MLPs to estimate the one-plane camera pose hypotheses, which are subsequently reweighed in a RANSAC manner to obtain the final camera pose. Because the neural one-plane pose minimizes the number of plane correspondences for adaptive pose hypotheses generation, it enables stable pose voting and reliable pose refinement in a few plane correspondences for the sparse-view inputs. In the experiments, we demonstrate that our NOPE-SAC significantly improves the camera pose estimation for the two-view inputs with severe viewpoint changes, setting several new state-of-the-art performances on two challenging benchmarks, *i.e.*, MatterPort3D and ScanNet, for sparse-view 3D reconstruction. The source code is released at <https://github.com/lceTTTb/NopeSAC> for reproducible research.

Index Terms—Planar 3D Reconstruction, Two-view Camera Pose Estimation, Sparse-view 3D Reconstruction, Deep Learning.

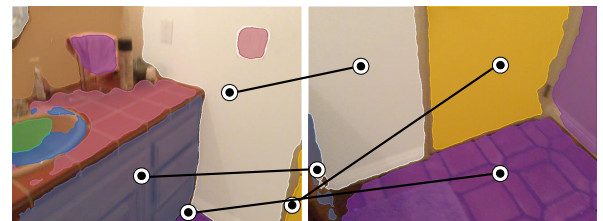
1 INTRODUCTION

TWO-VIEW 3D reconstruction is a fundamental and long-standing problem in computer vision, which is usually formulated to recover the relative camera pose and the scene geometry by feature correspondences [1]. Although such a classic formulation has been well established with keypoints in conventional Structure-from-Motion systems [2], [3], [4], [5], they are challenged by severe viewpoint changes and low-texture appearance of the captured images in the indoor scenes as shown in Fig. 1(a). In this paper, we are interested in addressing such a challenging configuration for two-view pose estimation and scene reconstruction, which is named as *sparse-view* 3D reconstruction in literature [6], [7], [8].

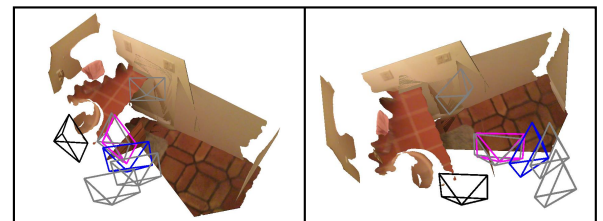
The *sparse-view images* are often resulted by large viewpoint changes up to scene scale in image capturing, which manifests as a low overlapping rate between the images. For instance, as shown in Fig. 1(a), even though adopting the state-of-the-art SuperGlue [9] for keypoint correspondences in the sparse-view image pair, it is infeasible for the well-known 5-point algorithm [10] because there are only 4 inliers among the 12 putative correspondences. However, when we carefully check the input sparse-view images from pixel level to object level with a focus on the *wall*, *floor*, and *door*, in our mind, these two images can be aligned in a unified 3D space. The pioneering works [7], [8] justified such an observation in learning-based reconstruction systems by relying on 3D plane correspondences, in which they formulate the challenging relative pose estimation problem in a voting form in accordance with the geometric correctness of



(a) SuperGlue Keypoint Correspondences [9]



(b) Plane Correspondences



(c) Camera Poses and Planar Reconstruction

Fig. 1. An illustration of the indoor sparse-view 3D reconstruction. (a) shows the keypoint correspondences of SuperGlue [9] including only 4 inliers (Green lines) and 8 outliers (Blue lines). (b) and (c) present the plane correspondences and reconstructed 3D planar scene of our NOPE-SAC from two sparse-view images. The **Black** frustum shows the ground truth camera of the second image. The **Pink**, **Gray**, and **Blue** frustums show the initial, the one-plane hypothetical, and the final cameras of the first image estimated by our NOPE-SAC.

- B. Tan, N. Xue and G.-S. Xia are with the School of Computer Science, Wuhan University, Wuhan, China, 430072.
- T. Wu is with the Department of Electrical and Computer Engineering, North Carolina State University, Raleigh, NC, USA, 27606.

(Corresponding author: Nan Xue.)

plane correspondences.

Voting the pose hypotheses by putative 3D plane correspondences in [7], [8] shares a similar spirit with the keypoint-based RANSAC framework [11] for pose estimation, but they use precomputed pose hypotheses instead of computing them from the inlier correspondences. To ensure that the precomputed pose hypotheses can cope with complicated pose distribution, the number of hypotheses would be large (*e.g.*, 1024 in *SparsePlane* [7]), which induced a contradiction between a large number of hypotheses and the small number of plane correspondences. For example, there are only 4 plane correspondences in Fig. 1(b) for hypotheses voting, thus being unstable and unreliable to distinguish the best hypothesis from the 1024 ones. To this end, a time-consuming continuous optimization with the assistance of keypoint correspondences is required [7] for accurate sparse-view 3D reconstruction. Although they achieved impressive reconstruction results, from the perspective of RANSAC [11], they ignored a key problem of pose hypotheses generation and are thus inflexible and computationally expensive for sparse-view 3D reconstruction.

In this paper, we pursue to formulate the camera pose estimation with pure plane correspondences in RANSAC to get rid of the fixed pose hypotheses. Considering the fact that explicitly modeling the relationship between the plane correspondences and the relative camera pose in the sparse-view setting would lead to ill-posed minimal problems [12], we leverage neural networks to encode the parameters of plane correspondences into a pose embedding space and learn to generate the pose hypotheses. We minimize the number of plane correspondences to 1 for the pose hypothesis generation, namely one-plane pose, and thus propose our *Neural One-Plane RANSAC* (NOPE-SAC) framework. With the one-plane pose generation, the number of pose hypotheses is significantly reduced to be the same as the number of plane correspondences. Consequently, the contradiction between the number of hypotheses and those of the supported inlier plane correspondences is largely alleviated, which makes it possible to fully utilize the information of plane correspondences for recovering accurate camera pose from sparse-view images without using post-processing steps such as the continuous optimization in [7].

We build our NOPE-SAC together with the plane detection and matching modules to establish a complete planar reconstruction system. More precisely, given two sparse-view images, our NOPE-SAC first detects 3D planes on each image and makes the plane correspondences by solving an optimal transport problem as in [9]. To start the pose estimation in RANSAC with a coarse initial camera pose, we leverage a convolutional neural network (ConvNet) for the learning of pose embedding which is then used to decode the initial pose. Then, the parameters of each plane correspondence are encoded together with the initial pose embedding to form a new pose embedding for the generation of one-plane pose hypotheses. Due to the flexibility issue of pose initialization from ConvNets, we present an arbitrary pose initialization module (AIM) that follows the auto-encoder structure to encode poses from other methods into embeddings. Next, with a coarse initial camera pose and N putative plane correspondences, our NOPE-SAC generates N one-plane pose hypotheses, which are then voted by the

geometric cost of the plane correspondences. Finally, the refined pose is estimated by fusing all hypotheses together with voting scores, and the holistic planar reconstruction is approached as the final output. Fig. 1 presents an illustrative example of our NOPE-SAC for the sparse-view input images. For the four plane correspondences predicted by the siamese network, our NOPE-SAC yields an initial pose (with the pink frustum) and four one-plane pose hypotheses (with the gray frustums), and then use the plane correspondences to vote and fuse the hypotheses (including the initial pose) for achieving a holistic 3D reconstruction.

In the experiments, we evaluate our NOPE-SAC on two indoor benchmark datasets, *i.e.*, Matterport3D [13] with sparse-view splits created by *SparsePlanes* [7] and ScanNet [14] with a more challenging split created by ourselves (see Sec. 5.1 for details). On both benchmarks, our NOPE-SAC achieves state-of-the-art performance in terms of pose estimation accuracy and planar 3D reconstruction precision. Compared to the prior arts (*e.g.*, *PlaneFormers* [8]), our NOPE-SAC pushed the accuracy of pose estimation on the Matterport3D dataset to 73.2% and 89.0% for translation and rotation (6.4% and 5.2% absolute improvements), the accuracy of pose estimation on the ScanNet dataset to 82.0% and 82.6% for translation and rotation (6.7% and 9.4% absolute improvements), and the Average Precision (AP) of 3D plane reconstruction to 43.29% on the Matterport3D and 39.39% on the ScanNet (5.76% and 4.75% absolute improvements). The comprehensive ablation studies further verified the design rationales of the proposed NOPE-SAC.

In summary, in this article, we present a novel approach, *i.e.*, NOPE-SAC, to address the challenging problem of sparse-view planar 3D reconstruction in a RANSAC framework, which fully takes the advantage of end-to-end learning of deep neural networks. By our NOPE-SAC, the neural one-plane pose hypotheses alleviate the contradiction between the number of the pose hypotheses and the 3D plane correspondences, thus improving the accuracy of camera pose estimation without incurring any offline optimization procedures. In performance, our method sets several new state-of-the-art performances on both the Matterport3D [13] and the ScanNet [14] datasets for pose estimation and holistic planar reconstruction. The comprehensive experimental analyzes also aligned benchmarking protocols for sparse-view 3D reconstruction.

2 RELATED WORK

2.1 Single-View 3D Reconstruction

One relevant task to indoor 3D reconstruction is to recover 3D scenes from single images. As one of the most widely used solutions, single-view depth estimation has been extensively studied [15], [16], [17], [18], [19] to pixel-wisely predict the depth values of the input images. Benefitting from the advances of deep learning and the richness of the training data for depth estimation [20], [21], we have witnessed their significant improvements in estimation accuracy and generalization ability.

Because the single-view depth estimation can only yield unstructured 3D point clouds, they would bring structural distortions into predictions for structured scenes, *e.g.*, the indoor scenes. To this end, some researchers propose to

directly predict 3D planes from a single image to reconstruct the geometry of structured scene [22], [23], [24], [25]. For example, Liu *et al.* [23] applied a two-stage instance segmentation framework to jointly detect plane instance masks and estimate 3D plane parameters for the single view planar reconstruction. Although these insightful methods work well for single-view indoor plane reconstruction, they can not recover the holistic scene because of the limited field of view in every single-view image.

In this paper, we take the merits of single-view planar 3D reconstruction and go further to the challenging sparse two-view configurations. We show that the estimated 3D planes from single-view images are favorable for both camera pose estimation and planar 3D reconstruction from the low-overlapping two-view images.

2.2 Two-View Camera Pose Estimation

Two-view 3D reconstruction is the most fundamental task in computer vision, which was formulated to solve the relative camera poses between the input images and estimate the scene geometry from the camera motions. The problem of camera pose estimation is the core of this task.

A common solution is to estimate camera poses from keypoint correspondences [26], [27], [28], [29], [30] relying on a typical 5-point solver [10] with a RANSAC [11] framework. Following this paradigm, there have been tremendous efforts on improving the performance of keypoint detection and matching by neural networks [9], [31], [32], [33], [34], [35]. As our study mainly focuses on the sparse-view configuration for two-view 3D reconstruction, such a common solution would be infeasible due to the fact of low-overlapping rate between the sparse-view inputs for feature correspondences.

Recently, some approaches leverage neural networks to directly estimate camera poses from feature cost volumes built up on dense pixel correspondences [36], [37], [38], [39]. Besides, Wei *et al.* [36] combined the traditional and learning-based methods by estimating dense pixel correspondences with a neural network and retrieving camera poses with the 5-point solver [10]. Although these learning-based methods have shown their excellent performances, they largely depend on sufficient image overlap to achieve motion cues from correspondences and thus are challenged by sparse-view indoor images with small overlapping rates.

Most recently, the problem of pose estimation from sparse-view indoor images has been extensively studied [6], [7], [8]. Due to the challenges of obtaining a sufficient number of inlier correspondences, these approaches use a large number of a-priori poses (by clustering the ground-truth camera poses) as the label space and formulate the problem of pose estimation to label scoring with respect to classification likelihoods and plane correspondences. Because a large number of a-priori poses would affect the flexibility and their estimation accuracy, these approaches have to adopt an optimization scheme for estimation refinement. Compared to those approaches, we show that although the number of 3D plane correspondences is very limited in sparse-view configuration, it works very well in a consensus sampling pipeline by generating the one-plane pose hypotheses and voting to obtain the accurate estimation of camera poses in end-to-end learning.

3 PLANAR CORRESPONDENCES PREPARATION

The overview of our proposed Nope-SAC for planar 3D reconstruction is illustrated in Fig. 2, which detects 3D planes from the two-view images and establishes the plane correspondences between views for camera pose estimation and planar 3D reconstruction. We focus on 3D plane detection and matching in this section and leave the key components for pose estimation in Sec. 4. With the estimated relative camera pose, the scene reconstruction is finally achieved by aligning the 3D plane correspondences between viewpoints.

3.1 3D Plane Instance Detection

Similar to [7], we define a plane instance as $\pi = \{\mathbf{n}, d, \mathcal{M}, \text{emb}\}$, where $\mathbf{n} \in \mathbb{R}^3$ and d are the plane normal and the offset from the plane to the camera center, $\mathcal{M} \in \mathbb{R}^{H \times W}$ is the plane segmentation mask (H and W are the image height and width, respectively.) and $\text{emb} \in \mathbb{R}^{256}$ is a plane appearance embedding.

We use the recent PlaneTR [25] as the 3D plane detection module for each input view with two main modifications: (1) the line segmentation branch in PlaneTR [25] is excluded to keep the simplicity; (2) the backbone network of PlaneTR [25] is replaced to ResNet-50 [40] for efficiency.

In computation, we use the output feature of the Transformer decoder in [25] as the plane appearance embedding and predict the normal and offset of each plane on top of the plane appearance embedding with a linear layer. The 3D plane detection module is supervised as:

$$\mathcal{L}_{\text{plane}} = \mathcal{L}_{\text{cls}} + 20\mathcal{L}_{\text{mask}} + \mathcal{L}_{\text{dice}} + \mathcal{L}_{\text{parm}} + 0.5\mathcal{L}_{\text{center}}, \quad (1)$$

where \mathcal{L}_{cls} , $\mathcal{L}_{\text{mask}}$, $\mathcal{L}_{\text{dice}}$, $\mathcal{L}_{\text{parm}}$ and $\mathcal{L}_{\text{center}}$ are the classification loss, the mask loss, the dice loss [41], the plane parameter loss and the plane center loss as used in [25], [42]. We refer readers to [25], [42] for more details.

3.2 Plane Matching

Denoted by $\Pi_1 = \{\pi_i^{(1)}\}_{i=1}^{K_1}$ and $\Pi_2 = \{\pi_j^{(2)}\}_{j=1}^{K_2}$ the plane sets from two view images, we aim to find an optimal partial assignment $A \in [0, 1]^{K_1 \times K_2}$ from Π_1 to Π_2 for plane matching, where K_1 and K_2 are the number of plane instances in two images. The optimal partial assignment A is solved as an Optimal Transport (OT) problem based on the scoring matrix $S \in \mathbb{R}^{K_1 \times K_2}$.

Scoring Matrix. Given the plane sets Π_1 and Π_2 , we compute the affinity matrices in terms of appearance and geometry and linearly add them as the final scoring matrix. For the affinity of plane appearance, we apply an Attentional Graph Neural Network used in [9] on the plane appearance embeddings to obtain two encoded sequence $E_1 \in \mathbb{R}^{K_1 \times 256}$ and $E_2 \in \mathbb{R}^{K_2 \times 256}$. Then, the appearance score matrix is computed by

$$S_e = E_1 E_2^T. \quad (2)$$

The geometric affinity is defined by the plane parameters between two 3D planes. Given an initial relative camera pose R, \mathbf{t} (see Sec. 4.1 for details), we first convert the 3D plane parameters of Π_1 to $\tilde{\Pi}_1$, the warped counterpart of

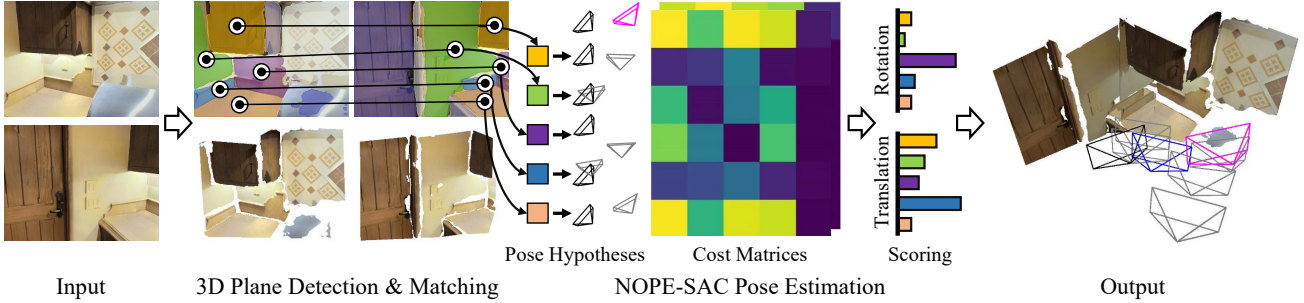


Fig. 2. Overview of the proposed NOPE-SAC. Our network first detects 3D planes (Sec. 3.1) and estimates plane correspondences (Sec. 3.2) from the input sparse-view images. Then, the final relative camera pose of the first image (**Blue** frustum) is voted from a coarse initial pose (**Pink** frustum) and a few one-plane poses (**Gray** frustum) according to the geometric cost of plane correspondences (Sec. 4). At last, the planar 3D reconstruction is achieved as the final output. The **Black** frustum shows the camera of the second image.

Π_1 under the coordinate frame of Π_2 , and then calculate the geometric affinity matrix by:

$$S_g(i, j) = -\lambda_1 \text{acos}(\tilde{n}_i^{(1)}, n_j^{(2)}) - \lambda_2 |\tilde{d}_i^{(1)} - d_j^{(2)}|, \quad (3)$$

where $\tilde{n}_i^{(1)}$ and $\tilde{d}_i^{(1)}$ are the i^{th} plane normal and offset in $\tilde{\Pi}_1$. $n_j^{(2)}$ and $d_j^{(2)}$ are the j^{th} plane parameters in Π_2 . λ_1 and λ_2 are set to 0.125 and 0.25 to balance the magnitude of the two terms.

Finally, the scoring matrix S can be calculated as:

$$S = S_e + S_g \quad (4)$$

Optimal Matching. Given a scoring matrix S , we apply a differentiable Sinkhorn Algorithm [43], [44] to output a soft assignment matrix A . Then, for a pair of planes $\{\pi_i^{(1)}, \pi_j^{(2)}\}$, they can be regarded as matched planes if $A(i, j)$ is the maximal score both in the i^{th} row and the j^{th} column of A , and $A(i, j)$ is larger than a fixed matching threshold (0.2 in this paper). We supervise the plane matching module with the loss defined in Eqn. (5). More precisely, let $\bar{A} \in \mathbb{R}^{(K_1+1) \times (K_2+1)}$ to be the soft assignment matrix augmented with dustbins and the expected soft assignment matrix $A = \bar{A}_{1:K_1, 1:K_2}$, the plane matching loss can be calculated as:

$$\begin{aligned} \mathcal{L}_{\text{match}} = & - \sum_{(i,j) \in \mathcal{A}} \log \bar{A}_{i,j} - \sum_{i \in \mathcal{I}} \log \bar{A}_{i, K_2+1} \\ & - \sum_{j \in \mathcal{J}} \log \bar{A}_{K_1+1, j}, \end{aligned} \quad (5)$$

where, $\mathcal{A} = \{(i, j)\}$ are the indices of ground truth matches. \mathcal{I} and \mathcal{J} are the indices of unmatched planes in two images respectively.

Correspondences Preparation for Pose Estimation. After the computation of optimal matching by the Sinkhorn layer, we extract a total number of M plane correspondences, denoted in the set $\mathbb{P} = \{(\mathcal{P}_m^{(1)}, \mathcal{P}_m^{(2)})\}_{m=1}^M$, where the superscript (i) indicates the viewpoint index. For each plane $\mathcal{P}_m^{(i)}$, we denote the normal and offset in $\mathbf{n}_m^{(i)} \in \mathbb{R}^3$ and $d_m^{(i)} \in \mathbb{R}_+$, respectively. With the plane correspondence set \mathbb{P} , we aim at estimating the relative camera pose in Sec. 4.

4 NOPE-SAC POSE ESTIMATION

Given the initial camera pose $\xi_0 = (R_0, \mathbf{t}_0)$ and a pair of matched planes $\mathcal{P}_m^{(1)}$ in the first-view image \mathcal{I}_1 and $\mathcal{P}_m^{(2)}$ in the second-view image \mathcal{I}_2 , the proposed NOPE-SAC learns the one plane pose in the embedding space of the initial camera pose ξ_0 and the plane correspondence $(\mathcal{P}_m^{(1)}, \mathcal{P}_m^{(2)})$. For a total of M putative plane matches, there will be M one-plane poses and we then learn to vote those one-plane pose hypotheses according to the geometric cost in the planar consensus set. Thanks to the pose hypotheses by NOPE-SAC only requiring one plane correspondence to yield a pose hypothesis, the imbalance issue between the number of hypotheses and the cardinal of the consensus set is largely alleviated for accurate pose estimation.

4.1 Camera Pose Initialization

In the consensus sampling pipelines for camera pose estimation, a coarse estimation is required to kick off the estimation of pose parameters. Different from the keypoint-based RANSAC (and its variants) that did the coarse estimation by randomly sampling a small subset of keypoint correspondences, it would be more challenging to obtain the coarse estimation from plane correspondences by an explicit mathematical model. To this end, we resort to the convolutional neural network to learn the initial pose ξ_0 from the feature volume of image \mathcal{I}_1 and \mathcal{I}_2 .

Pose Regression Network. We take ResNet-50 [40] as our backbone network for the initial pose regression. Given two input images \mathcal{I}_1 and \mathcal{I}_2 of which they are with the spatial size of $H \times W$, the output backbone features \mathcal{F}_1 and \mathcal{F}_2 are taken to build a 4D affinity volume $V \in \mathbb{R}^{(h \times w) \times (h \times w)}$ by

$$V(\mathbf{p}, \mathbf{p}') = \frac{\exp(\mathcal{F}_2^T(\mathbf{p})\mathcal{F}_1^T(\mathbf{p}'))}{\sum_{\mathbf{p}} \exp(\mathcal{F}_2^T(\mathbf{p})\mathcal{F}_1^T(\mathbf{p}'))}, \quad (6)$$

for any pair of pixels \mathbf{p} and \mathbf{p}' in the coordinates of \mathcal{F}_1 and \mathcal{F}_2 , where $h = H/s$, $w = W/s$, and $s = 32$ is the stride of backbone network. The computation of V is similar to [7], however, we choose to directly predict the pose parameters instead of learning the classification likelihood with respect to a set of discrete pose templates as the formulation of classification would hurt the end-to-end learning for camera pose estimation.

To predict the initial camera pose $\xi_0 = (R_0, \mathbf{t}_0) \in \text{SE}(3)$, the affinity volume is rearranged to $\mathcal{V} \in \mathbb{R}^{hw \times hw}$, and

is then transformed respectively by 6 convolutional layers (including BatchNorm and LeakyReLU) and a linear layer to yield two feature embeddings, $f_r^{(0)}, f_t^{(0)} \in \mathbb{R}^{256}$ for the rotation R_0 and translation \mathbf{t}_0 . Here, the stride of each even-numbered convolution operation is set to 2 to reduce the feature size. With $f_r^{(0)}, f_t^{(0)}$, it is straightforward to predict the rotation and translation by linear layers $\text{LinearRot}(\cdot)$ and $\text{LinearTrans}(\cdot)$ with

$$\mathbf{q}_0 = \text{LinearRot}(f_r^{(0)}), \mathbf{t}_0 = \text{LinearTrans}(f_t^{(0)}), \quad (7)$$

where $\mathbf{q}_0 \in \mathbb{R}^4$ is the unit quaternion of the rotation matrix that satisfies $\|\mathbf{q}_0\|_2 = 1$. The weights of $\text{LinearRot}(\cdot)$ and $\text{LinearTrans}(\cdot)$ are optimized by the MSE (Mean-Square Error) loss

$$\mathcal{L}_{\text{cam}}^{\text{init}} = \|\mathbf{q}_0 - \mathbf{q}^{gt}\|_2^2 + \|\mathbf{t}_0 - \mathbf{t}^{gt}\|_2^2, \quad (8)$$

where \mathbf{q}^{gt} and \mathbf{t}^{gt} are the ground truths of the rotation (in unit quaternions) and translation between the input images $(\mathcal{I}_1, \mathcal{I}_2)$.

Besides predicting the initial camera poses, the embedding $f_r^{(0)}$ and $f_t^{(0)}$ plays a vital role in our proposed NOPE-SAC because it generates the pose hypotheses by the embedding vectors of initial poses and plane correspondences. Thus, there would be an issue of inflexibility for the initial poses that do not come from the convolutional pose estimation network. We present an Arbitrary Initialization Module (AIM) that reconstructs a given camera pose via auto-encoding to cope with this situation.

Arbitrary Initialization Module. We featurize any given quaternion \mathbf{q}^* (of rotation $R^* \in \text{SO}(3)$) and translation $\mathbf{t}^* \in \mathbb{R}^3$ in an auto-encoding manner by:

$$\begin{aligned} f_r^* &= \text{RotEnc}(\mathbf{q}^*), f_t^* = \text{TransEnc}(\mathbf{t}^*), \\ \tilde{\mathbf{q}}^* &= \text{LinearRot}(f_r^*), \tilde{\mathbf{t}}^* = \text{LinearTrans}(f_t^*), \end{aligned} \quad (9)$$

where $\text{RotEnc}(\cdot)$ and $\text{TransEnc}(\cdot)$ are the encoders for rotation and translation by MLPs, $\text{LinearRot}(\cdot)$ and $\text{LinearTrans}(\cdot)$ are the shared layers defined in Eqn. (7) to reconstruct the camera poses by

$$\mathcal{L}_{\text{rec}} = \|\tilde{\mathbf{q}}^* - \mathbf{q}^*\|_2^2 + \|\tilde{\mathbf{t}}^* - \mathbf{t}^*\|_2^2. \quad (10)$$

For the training of AIM, we randomly sample the rotations and translations from the uniform distribution, please move to Section 5.3 for the details.

4.2 Camera Pose Refinement

With the initial camera pose $\xi_0 = (R_0, \mathbf{t}_0)$ and its corresponding feature embedding $f_r^{(0)}$ and $f_t^{(0)}$, we present the core of NOPE-SAC that consists of the following steps: (1) One-plane Pose Hypotheses Generation, (2) Hypotheses Scoring and (3) Pose Refinement based on the M 3D plane correspondences $\mathbb{P} = \{\mathcal{P}_m\}_{m=1}^M$. For each plane correspondence \mathcal{P}_m , the normal vector (3D real vectors) and the offset (real scalars) from the plane to the camera center in the input images \mathcal{I}_1 and \mathcal{I}_2 are denoted by $(\mathbf{n}_m^{(1)}, d_m^{(1)})$ and $(\mathbf{n}_m^{(2)}, d_m^{(2)})$, respectively.

One-plane Pose Hypotheses Generation. For the m -th 3D plane correspondence $\mathcal{P}_m^{(1)} = (\mathbf{n}_m^{(1)}, d_m^{(1)})$ in \mathcal{I}_1 and $\mathcal{P}_m^{(2)} =$

TABLE 1
Detailed architecture of MLPs used in NOPE-SAC Pose Estimation Module. For each MLP, the corresponding equation, notation, the number of linear layers, the channel dimensions of inputs and outputs, and the activation functions are listed.

Equation	Notation	# Layers	# Channels In	# Channels Out	Activation
Eqn. (9)	RotEnc / TransEnc	6	256	256	ReLU
Eqn. (11)	\mathcal{G}	1	8	1024	ReLU
		4	1024	1024	ReLU
		1	1024	1024	-
		2	1024	1024	ReLU
1	1024	1024	-		
Eqn. (12)	\mathcal{E}_r	1	1024	512	ReLU
		4	512	512	ReLU
		1	512	256	-
Eqn. (12)	\mathcal{E}_t	1	1280	1024	ReLU
		1	1024	1024	ReLU
		1	1024	1024	-
		1	1024	512	ReLU
		4	512	512	ReLU
		1	512	256	-
Eqn. (13)	$\mathcal{D}_r / \mathcal{D}_t$	2	512	512	ReLU
		1	512	256	ReLU

$(\mathbf{n}_m^{(2)}, d_m^{(2)})$ in \mathcal{I}_2 , we leverage an MLP layer $\mathcal{G}(\cdot) : \mathbb{R}^8 \mapsto \mathbb{R}^{1024}$ to embed the correspondence by

$$g_m = \mathcal{G}(\tilde{\mathbf{n}}_m^{(1)} \oplus \tilde{d}_m^{(1)} \oplus \mathbf{n}_m^{(2)} \oplus d_m^{(2)}), \quad (11)$$

where $\tilde{\mathbf{n}}_m^{(1)}$ and $\tilde{d}_m^{(1)}$ are the warped normal of $\mathbf{n}_m^{(1)}$ and offset of $d_m^{(1)}$ by the relative camera pose (R_0, \mathbf{t}_0) , \oplus is the concatenation operation. Here, the warped plane parameters by the initial camera pose could be regarded as a kind of normalization to facilitate the learning of plane correspondence embedding in neural networks.

With the correspondence embedding g_m , we further transform it to the rotation feature $e_m^r \in \mathbb{R}^{256}$ and the translation feature $e_m^t \in \mathbb{R}^{256}$ by two MLPs \mathcal{E}_r and \mathcal{E}_t as

$$\begin{aligned} e_m^r &= \mathcal{E}_r(g_m), \\ e_m^t &= \mathcal{E}_t(g_m \oplus e_m^r). \end{aligned} \quad (12)$$

Then, we concatenate e_m^r and e_m^t with the embedding $f_r^{(0)}$ and $f_t^{(0)}$ of the initial camera pose, and transform the concatenated embedding by two MLP layers $\mathcal{D}_r(\cdot) : \mathbb{R}^{512} \mapsto \mathbb{R}^{256}$ and $\mathcal{D}_t(\cdot) : \mathbb{R}^{256} \mapsto \mathbb{R}^{256}$ to yield the one-plane pose embedding f_m^r and f_m^t as

$$\begin{aligned} f_m^r &= \mathcal{D}_r(f_r^{(0)} \oplus e_m^r), \\ f_m^t &= \mathcal{D}_t(f_t^{(0)} \oplus e_m^t). \end{aligned} \quad (13)$$

Finally, to obtain the one-plane rotation and translation for the m -th plane correspondence, we leverage the linear layers $\text{LinearRot}(\cdot)$ and $\text{LinearTrans}(\cdot)$ defined in Eqn. (9) as the shared headnets by

$$\begin{aligned} \mathbf{q}^{(m)} &= \text{LinearRot}(f_m^r), \\ \mathbf{t}^{(m)} &= \text{LinearTrans}(f_m^t), \end{aligned} \quad (14)$$

where $\mathbf{q}^{(m)}$ and $\mathbf{t}^{(m)}$ are the predicted quaternion of rotation and the translation.

Hypotheses Scoring Layer. Next to the pose hypotheses generation, we compute the geometric cost for each predicted rotation and translation. For each pose hypothesis $R^{(m)}$ and $\mathbf{t}^{(m)}$, the rotation cost $c_r^{(m)} \in \mathbb{R}^M$ and translation

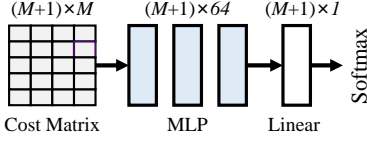


Fig. 3. An illustration of the Hypotheses Scoring Layer. The input cost matrix is first passed through an MLP layer and then converted to the scores with a linear layer and Softmax operation. The top line shows the output dimensions of each step.

cost $c_t^{(m)} \in \mathbb{R}^M$ throughout all M plane correspondences are calculated by

$$\begin{aligned} c_r^{(m)} &= \left(\|\mathbf{n}_{i,m}^{(1)} - \mathbf{n}_i^{(2)}\|_2 \right)_{i=1}^M \\ c_t^{(m)} &= \left(\|d_{i,m}^{(1)} \mathbf{n}_{i,m}^{(1)} - d_i^{(2)} \mathbf{n}_i^{(2)}\|_2 \right)_{i=1}^M, \end{aligned} \quad (15)$$

where $\mathbf{n}_{i,m}^{(1)}$ and $d_{i,m}^{(1)}$ are the warped normal and offset of the plane $\mathcal{P}_i^{(1)}$ by the m -th pose hypothesis. By including the costs of initial pose (R_0, \mathbf{t}_0) , there will be two cost matrices $C_r \in \mathbb{R}^{(M+1) \times M}$ and $C_t \in \mathbb{R}^{(M+1) \times M}$, which are then fed into two parallel Hypotheses Scoring Layers to yield the rotation scores $\mathbf{w}_r = (w_r^{(0)}, \dots, w_r^{(M)})$ and the translation scores $\mathbf{w}_t = (w_t^{(0)}, \dots, w_t^{(M)})$, respectively. Here, the sum of scores is equal to 1 and we use the Softmax operation in our implementation. As shown in Fig. 3, each Hypotheses Scoring Layer consists of an MLP layer (including 3 linear layers with ReLU activations and 64 channels per layer) and one linear layer for score prediction.

To train the scoring layer, we design a scoring loss to supervise the learning of pose scores dynamically. Let i and j be the indices of rotation and translation in all pose hypotheses $\{R^{(m)}\}_{m=0}^M$ and $\{t^{(m)}\}_{m=0}^M$ that are closest to the ground truth camera poses. Then, the heuristic scoring loss can be calculated as:

$$\mathcal{L}_{\text{score}} = \|1 - w_r^i\|_1 + 2\|1 - w_t^j\|_1 + \frac{10}{M} \sum_{m=1}^M c_t^{(m)}(m), \quad (16)$$

where w_r^i and w_t^j are the predicted rotation and translation scores, and $c_t^{(m)}(m)$ means the translation cost of plane correspondence \mathcal{P}_m with the m -th pose hypothesis.

Final Pose Estimation. Following the hypotheses scoring layer, we present a *Soft* fusion strategy by default to fuse all the pose hypotheses to obtain the final pose. In detail, we use the predicted scores $\mathbf{w}_r, \mathbf{w}_t$ to obtain the embedding of the final pose by

$$f_r = \sum_{i=0}^M w_r^i f_r^{(i)}, f_t = \sum_{i=0}^M w_t^i f_t^{(i)}, \quad (17)$$

and leverages the layers $\text{LinearRot}(\cdot)$ and $\text{LinearTrans}(\cdot)$ again as the shared pose predictors to obtain the final pose $\xi_{\text{ref}} = (\mathbf{q}_{\text{ref}}, \mathbf{t}_{\text{ref}})$. We denote the computation of the camera pose refinement module by

$$\xi_{\text{ref}} = \text{PoseRef}(\xi_0, \mathbb{P}; \Theta), \quad (18)$$

where ξ_0 and \mathbb{P} are the required input of the initial pose and the plane correspondences, and Θ indicates the parameters of the neural networks.

Apart from the *Soft* fusion scheme, there are three representative alternatives to get the final refined pose from pose hypotheses, which are summarized as follows:

- *Avg*: It treats all pose hypotheses equally and sets all scores used in Eqn. (17) to be $\frac{1}{M+1}$.
- *Min-Cost*: It selects the minimal-cost rotation/translation hypothesis according to Eqn. (15) and discard all the remaining hypotheses.
- *Max-Score*: It takes the maximal-score rotation/translation hypothesis according to the hypotheses scoring layer as the final pose prediction.

If not explicitly stated, we use the *Soft* fusion strategy in all experiments, and we analyze these fusion strategies in the ablation study.

We supervise the final pose prediction with the MSE loss. Because there are two initial pose predictions ξ_0^{reg} (from the regression branch) and ξ_0^{rec} (from the Arbitrary Initialization Module), by taking the predicted plane correspondences \mathbb{P}_{pred} and the ground-truth \mathbb{P}_{gt} into account during training, there will be four predictions of the refined camera pose for the *Soft* fusion scheme. We compute the loss functions $\mathcal{L}_{\text{cam}}^{\text{soft}}$ and $\mathcal{L}_{\text{score}}$ for the refinement module similar to Eqn. (8) and Eqn. (16), but the four predictions are all taken in the computation. To avoid instability during training, the *Avg* fusion strategy is also involved to compute a loss function $\mathcal{L}_{\text{cam}}^{\text{avg}}$. Finally, the total loss function of the refinement module is denoted by

$$\mathcal{L}_{\text{cam}}^{\text{ref}} = \mathcal{L}_{\text{cam}}^{\text{soft}} + \mathcal{L}_{\text{cam}}^{\text{avg}} + 0.01\mathcal{L}_{\text{score}}. \quad (19)$$

To train the NOPE-SAC for pose estimation, we linearly add the loss functions $\mathcal{L}_{\text{cam}}^{\text{init}}, \mathcal{L}_{\text{rec}}$ and $\mathcal{L}_{\text{cam}}^{\text{ref}}$ by

$$\mathcal{L}_{\text{pose}} = \mathcal{L}_{\text{cam}}^{\text{init}} + \mathcal{L}_{\text{rec}} + \mathcal{L}_{\text{cam}}^{\text{ref}} \quad (20)$$

as the total loss for the camera pose estimation.

5 EXPERIMENTS AND ANALYSIS

This section presents the experiments of our NOPE-SAC.

5.1 Datasets

Matterport3D Dataset. We use the sparse view dataset based on Matterport3D [13] with ground truth camera poses and plane annotations generated by [7], which contains 31932, 4707, and 7996 image pairs for training, validation, and testing. The size of each image is 480×640 .

ScanNet Dataset. We create a new sparse view split on the indoor ScanNet [14] video dataset with plane annotations generated by [23]. The image size is 480×640 . We randomly sample 17237/4051 image pairs from 1210/303 non-overlapping scenes for training/testing. The frame interval within a sampled image pair is at least 20 and 40 frames in the training and test sets, respectively.

Dataset Analysis. We first analyze the image overlap on the Matterport3D [13] and the ScanNet [14] datasets. As shown in the top row of Fig. 4, our split on the ScanNet dataset contains more low-overlap image pairs than the split on the Matterport3D dataset created by [7]. Further, we visualize the distributions of rotations (represented as

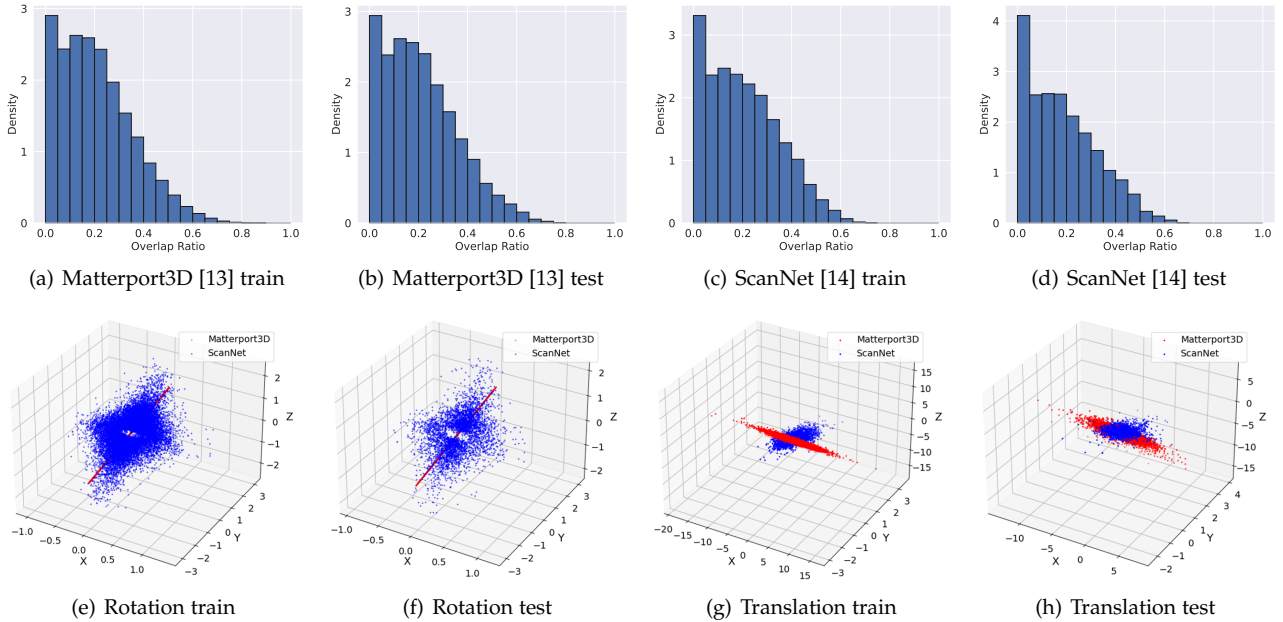


Fig. 4. Dataset analysis of the sparse-view split on the Matterport3D [13] and the ScanNet [14] datasets. The top row shows the image overlap ratio on the training and test set of two datasets (from left to right, the average percentages of image overlap are 20.9%, 21.0%, 20.6% and 18.6%). At the bottom, we visualize the rotation and translation distributions on the ScanNet (Blue dot) and the Matterport3D (Red dot) datasets.

rotation vectors) and translations on the training and test set of these two datasets. As shown in the bottom row of Fig. 4, although the translation range on the ScanNet dataset is smaller than the Matterport3D dataset, the rotation distribution on the ScanNet dataset is much more complex than the Matterport3D dataset, which makes our split on the ScanNet dataset more challenging.

5.2 Evaluation Metrics

Metrics for Camera Pose Estimation. We evaluate camera poses with the rotation angle error and the translation distance error as used in [7], [36], [37]. The reported metrics include the mean and median errors, and the percentage of errors lower than a threshold.

Metrics for 3D Plane Reconstruction. According to SparsePlanes [7], the matched planes are merged together and all 3D planes from two views are converted to the same coordinate system. Then, the reconstructed full scene is evaluated like a detection problem with the metric of average precision (AP). A reconstructed 3D plane is regarded as a true positive if the following conditions of (1) its mask IoU ≥ 0.5 , (2) its plane normal angle error in degree is less than α° , and (3) its plane offset error in meters is less than β are all satisfied.

5.3 Implementation Details

Our NOPE-SAC is implemented with Detectron2 [45] and the AdamW optimizer [46] is used for training with a batch size of 16. Because the sparse-view planar 3D reconstruction consists of multiple neural modules for the 3D plane detection and matching, the camera pose initialization (including the initial pose regression and the arbitrary pose initialization), and the pose refinement with one-plane pose hypotheses, we train the whole network in three stages on

the Matterport3D [13] training set. In the first stage, only the 3D plane detection module is optimized for 12k iterations with the learning rate of 10^{-4} . Then, we add the plane matching module, the initial pose regression network, and the arbitrary initialization module for the second stage of training in 50K iterations. The initial learning rate in this training stage is also 10^{-4} , and we use the multi-step learning rate schedule to adjust the learning rate at the milestones of 34k and 44k iterations with the decay factor of 0.1. In the last stage, we add the camera pose refinement module in training for a total of 14k iterations. The learning rate in this stage is initialized to 10^{-4} for the first 6k iterations and is decayed to 10^{-5} for the last 8k iterations.

On the ScanNet [14] dataset, we finetune the model trained on the Matterport3D dataset with two additional stages. In the first stage, we train the 3D plane detection module, the plane matching module, the initial pose regression network, and the arbitrary initialization module for 20K iterations. The initial learning rate is set to 10^{-4} and divided by 10 after 4.4K iterations. In the second stage, we add the camera pose refinement module and train the whole network for 15K iterations. The initial learning rate is set to 10^{-4} and divided by 10 after 2.2K iterations.

When training the arbitrary initialization module (AIM), we first represent the input rotation as a rotation vector $\mathbf{v}^* \in \mathbb{R}^3$. Then, we randomly sample each axis of \mathbf{v}^* and the input translation $\mathbf{t}^* \in \mathbb{R}^3$ from the uniform distribution $U(-2.5, 2.5)$. At last, the sampled rotation vector \mathbf{v}^* is converted to a unit quaternion \mathbf{q}^* as used in Eqn. 9.

5.4 Baseline Configurations

We compare our method with the state-of-the-art learning solutions including SparsePlanes [7] and PlaneFormers [8] for pose estimation and planar 3D reconstruction, as well as a keypoint-based solution built on the top-performing key-

TABLE 2
Comparison of camera poses on the Matterport3D [13] dataset and the ScanNet [14] dataset.

Method	Translation					Rotation				
	Med. ↓	Mean ↓	(≤1m) ↑	(≤0.5m) ↑	(≤0.2m) ↑	Med. ↓	Mean ↓	(≤ 30°) ↑	(≤ 15°) ↑	(≤ 10°) ↑
Matterport3D dataset										
SuperGlue [9]	-	-	-	-	-	3.88	24.17	77.8%	71.0%	65.7%
SparsePlanes [7]	0.63	1.15	66.6%	40.4%	11.9%	7.33	22.78	83.4%	72.9%	61.2%
PlaneFormers [8]	0.66	1.19	66.8%	36.7%	8.7%	5.96	22.20	83.8%	77.6%	68.0%
SparsePlanes-TR [7], [25]	0.61	1.13	67.3%	41.7%	12.2%	6.87	22.17	83.8%	74.5%	63.3%
PlaneFormers-TR [8], [25]	0.64	1.17	67.9%	38.7%	8.9%	5.28	21.90	83.9%	79.0%	70.8%
NOPE-SAC-Cls (ours)	0.66	1.20	65.6%	37.9%	9.8%	2.98	19.68	84.9%	83.1%	80.2%
NOPE-SAC-Reg (ours)	0.52	0.94	73.2%	48.3%	16.2%	2.77	14.37	89.0%	86.9%	84.0%
ScanNet dataset										
SuperGlue [9]	-	-	-	-	-	10.90	31.00	67.8%	56.0%	48.4%
SparsePlanes [7]	0.56	0.81	73.7%	44.6%	10.7%	15.46	33.38	70.5%	48.7%	28.0%
PlaneFormers [8]	0.55	0.81	75.3%	45.5%	11.3%	14.34	32.08	73.2%	52.1%	32.3%
SparsePlanes-TR [7], [25]	0.57	0.82	73.4%	43.6%	10.1%	14.57	32.36	72.8%	51.2%	30.1%
PlaneFormers-TR [8], [25]	0.53	0.79	76.2%	47.0%	11.4%	13.81	31.58	74.5%	54.1%	33.6%
NOPE-SAC-Cls (ours)	0.49	0.76	77.5%	50.9%	14.1%	9.01	27.84	77.9%	69.5%	55.1%
NOPE-SAC-Reg (ours)	0.41	0.65	82.0%	59.1%	21.2%	8.27	22.12	82.6%	73.2%	59.5%

TABLE 3

Detailed camera pose comparison with SparsePlanes-TR [7], [25] on the Matterport3D [13] dataset and the ScanNet [14] dataset. 'Cls.' Top-1' means the Top-1 classification pose of SparsePlanes [7]. 'Con.' means the continuous optimization proposed by SparsePlanes.

Method	Translation			Rotation		
	Med. ↓	Mean ↓	(≤0.5m) ↑	Med. ↓	Mean ↓	(≤ 15°) ↑
Matterport3D dataset						
Cls. Top-1	0.90	1.40	21.1%	7.65	24.57	71.7%
[7], [25] w/o Con.	0.88	1.35	21.9%	7.17	22.36	74.6%
[7], [25]	0.61	1.13	41.7%	6.87	22.17	74.5%
NOPE-SAC-Cls	0.66	1.20	37.9%	2.98	19.68	83.1%
ScanNet dataset						
Cls. Top-1	0.56	0.83	43.9%	15.21	33.16	49.5%
[7], [25] w/o Con.	0.55	0.83	44.2%	14.55	32.36	51.3%
[7], [25]	0.57	0.82	43.6%	14.57	32.36	51.2%
NOPE-SAC-Cls	0.49	0.76	50.9%	9.01	27.84	69.5%

point matcher, SuperGlue [9]. For the SparsePlanes [7] and PlaneFormers [8], we additionally set two variant baselines to compare the performance gain with the same 3D plane detection module.

SparsePlanes and SparsePlanes-TR. SparsePlanes [7] is the first sparse-view planar 3D reconstruction approach. Given a set of precompute pose hypotheses, it detects 3D planes in each view and predicts the likelihood of the precomputed set of camera poses by deep neural networks. Then, a discrete optimization problem is solved to obtain the optimal plane correspondences and the camera pose by taking the geometric correctness and embedding consistency between 3D planes across views, as well as the classification likelihood into account. Following the discrete optimization, a continuous optimization problem is formulated to refine the camera pose with the assistance of SIFT [26] keypoints. Since the 3D plane detection modules between SparsePlanes [7] and NOPE-SAC are different, we build a variant baseline SparsePlanes-TR to ensure the fairness of comparisons, in which we replace the plane detection module to PlaneTR [25] as our network used. Because the official implementation of SparsePlanes [7] did not provide results on the ScanNet [14] dataset, we train these baselines

on the ScanNet [14] dataset by ourselves.

PlaneFormers and PlaneFormers-TR. PlaneFormers [8] is the prior art developed based on SparsePlanes [7], which selects Top-9 classification poses from [7] as hypotheses. For each pose hypothesis, PlaneFormers jointly estimates the pose score and plane matching cost with a neural network. Finally, the pose with the best score is selected and refined with an extra estimated pose residual, and the plane correspondences are achieved by conducting an offline Hungarian algorithm on the matching cost. Like SparsePlane [7], we implemented the results of PlaneFormers on the ScanNet [14] dataset by ourselves. In PlaneFormers-TR, we use the planes detected by PlaneTR [25] as our network used.

SuperGlue. It is a strong baseline for keypoints detection and matching with neural networks. The camera poses are then calculated from matched keypoints with '5-point solver [10] + RANSAC [11]'. Since SuperGlue [9] lacks scale information in translations, we do not report its translation errors. In case SuperGlue fails to estimate camera poses, we set its rotation results as identity matrices like [7]. For the results of plane reconstruction, we use the ground truth scales in translations and match planes detected by PlaneTR [25] with our plane matching module.

5.5 Comparison of Camera Pose Estimation

We evaluate our NOPE-SAC with the regressed initial poses, namely NOPE-SAC-Reg, which is the main version of our proposed method. We also evaluate a variant of our NOPE-SAC which directly uses the Top-1 a-priori pose with a classification module of SparsePlanes [7] as initial poses, namely NOPE-SAC-Cls.

Quantitative Results. We first compare the performance of rotation estimation. As shown in Tab. 2, both our NOPE-SAC-Reg and Nope-SAC-Cls significantly outperform all baselines on both two datasets especially when the rotation threshold is small, *e.g.*, 84.0% (NOPE-SAC-Reg) *v.s.* 63.3% (SparsePlanes-TR) with the threshold of 10° on the Matter-



Fig. 5. Qualitative results of the refined poses and plane correspondences on the Matterport3D [13] dataset (first three rows) and the ScanNet [14] dataset (last three rows). The **Pink**, **Blue** and **Red** frustums show the initial, the refined, and the ground truth cameras of the first image respectively. **Gray** frustums show the one-plane pose hypotheses of the first image generated from plane correspondences. **Black** frustums show the camera of the second image.

port3D [13] dataset. Then, we further evaluate the translation results. When compared with SparsePlanes-TR [7], [25] and PlaneFormers-TR [8], [25] which use the a-priori classification poses, our NOPE-SAC-ClS performs slightly worse than them on the Matterport3D [13] dataset but outperforms them on the more challenging ScanNet [14] dataset.

With a further comparison to SparsePlanes-TR [7], [25] as shown in Tab. 3, we find that the improvement of translation estimation for SparsePlanes-TR [7], [25] largely depends on its keypoint-based continuous optimization. Although they are well-performing on the MatterPort3D [13] dataset, the performance of continuous optimization dramatically degenerates on the ScanNet [14] dataset because it is much more difficult to achieve good keypoint matches on the ScanNet dataset (as shown in Fig. 1(a)). By contrast, our NOPE-SAC-ClS consistently improves the initial poses with only the plane correspondences on both datasets.

Qualitative Results. Fig. 5 shows the pose estimation results of our NOPE-SAC from two different viewpoints (last two columns) on the Matterport3D [13] and the ScanNet [14] datasets. As described in Sec. 4, we compute one-plane pose hypotheses (**Gray** frustums) from estimated plane correspondences (the third column). Despite the outlier poses

caused by incorrect correspondences and inaccurate plane parameters, NOPE-SAC effectively achieved the final refined pose (**Blue** frustum) from all one-plane pose hypotheses (**Gray** frustums) and the initial pose (**Pink** frustum).

5.6 Comparison of 3D Planar Reconstruction

We evaluate two versions of our method named NOPE-SAC-Reg and NOPE-SAC-ClS as described in Sec. 5.5 on the Matterport3D [13] and ScanNet [14] datasets.

Quantitative Results. We evaluate our method with initial (Init.) and refined (Ref.) poses, and compare with baselines under various plane offset and normal error thresholds from loose to strict. As shown in Tab. 4, Our NOPE-SAC-Reg achieves state-of-the-art performance especially under the strictest settings with ‘Offset \leq 0.2m’ and ‘Normal \leq 5 $^\circ$ ’ on both Matterport3D [13] and ScanNet [14] datasets. When compared with SparsePlanes-TR [7], [25] which also uses classification poses, our NOPE-SAC-ClS effectively improves the reconstruction performance (e.g., from 25.21 to 30.25 with offset \leq 0.5m and normal \leq 10 $^\circ$ on the ScanNet dataset). Those performance gains confirmed the superiority of our proposed NOPE-SAC.

Qualitative Results. Fig. 6 visualizes the 3D plane reconstruction results by different approaches on the Matter-

TABLE 4

Average Precision (AP) of 3D plane reconstruction conditioned with mask IoU, normal angle error, and offset distance error. The threshold of mask IoU is fixed to 0.5. ‘All’ means we consider all three conditions. ‘-Offset’ and ‘-Normal’ mean we ignore the offset and the normal conditions respectively. ‘Con.’ means the continuous optimization proposed by SparsePlanes [7].

Method	Offset \leq 1m, Normal \leq 30°			Offset \leq 0.5m, Normal \leq 15°			Offset \leq 0.2m, Normal \leq 5°		
	All	-Offset	-Normal	All	-Offset	-Normal	All	-Offset	-Normal
Matterport3D dataset									
SuperGlue-TR [9], [25]	39.51	44.11	44.08	28.98	37.53	34.40	11.29	21.87	17.27
SparsePlanes [7] w/o Con.	35.87	42.13	38.80	23.36	35.34	27.48	8.07	17.28	12.99
SparsePlanes [7]	36.02	42.01	39.04	23.53	35.25	27.64	6.76	17.18	11.52
PlaneFormers [8]	37.62	43.19	40.36	26.10	36.88	29.99	9.44	18.82	14.78
SparsePlanes-TR [7], [25] w/o Con.	39.91	46.50	42.53	27.37	40.79	31.03	9.99	22.80	14.64
SparsePlanes-TR [7], [25]	40.35	46.39	43.03	27.81	40.65	31.38	9.02	22.80	13.66
PlaneFormers-TR [8], [25]	41.87	47.50	44.43	30.78	42.82	34.03	12.45	25.98	17.34
NOPE-SAC-Cls Init. (ours)	38.94	46.60	41.96	26.17	40.48	29.89	9.89	22.55	14.29
NOPE-SAC-Cls Ref. (ours)	41.92	48.18	44.01	31.36	44.24	34.01	13.59	30.05	17.45
NOPE-SAC-Reg Init. (ours)	40.07	46.03	43.59	26.78	36.76	31.95	10.09	19.09	15.55
NOPE-SAC-Reg Ref. (ours)	43.29	49.00	45.32	32.61	44.94	35.36	14.25	30.39	18.37
ScanNet dataset									
SuperGlue-TR [9], [25]	33.20	33.77	43.40	22.78	24.94	36.72	4.35	6.19	19.33
SparsePlanes [7] w/o Con.	33.20	34.12	40.74	22.89	25.62	33.67	3.03	4.52	17.17
SparsePlanes [7]	33.08	34.12	40.51	21.69	25.59	32.20	2.52	4.50	14.85
PlaneFormers [8]	34.64	35.47	41.37	24.48	27.19	34.69	3.93	5.52	18.58
SparsePlanes-TR [7], [25] w/o Con.	35.56	36.51	42.14	26.01	29.61	35.12	3.96	6.10	18.59
SparsePlanes-TR [7], [25]	35.32	36.50	41.92	24.71	29.55	33.50	3.21	6.07	15.32
PlaneFormers-TR [8], [25]	36.82	37.87	43.01	27.41	30.72	36.31	4.83	7.02	19.94
NOPE-SAC-Cls Init. (ours)	35.41	36.68	42.44	25.21	28.78	34.96	3.84	5.74	18.66
NOPE-SAC-Cls Ref. (ours)	38.23	39.36	43.27	30.25	34.15	36.93	6.23	9.57	20.56
NOPE-SAC-Reg Init. (ours)	36.39	37.35	43.15	25.59	28.54	36.06	4.59	6.41	19.92
NOPE-SAC-Reg Ref. (ours)	39.39	40.30	43.88	31.21	34.89	37.88	6.74	10.10	21.41

TABLE 5

Ablation studies for NOPE-SAC camera pose refinement.

Method	Translation					Rotation				
	Med. ↓	Mean ↓	(\leq 1m) ↑	(\leq 0.5m) ↑	(\leq 0.2m) ↑	Med. ↓	Mean ↓	(\leq 30°) ↑	(\leq 15°) ↑	(\leq 10°) ↑
Matterport3D dataset										
Initial Pose	0.69	1.08	65.0%	37.0%	10.1%	11.16	21.49	81.3%	60.5%	46.5%
Nume-Ref-I	0.52	1.06	69.2%	48.5%	19.1%	7.17	21.96	79.8%	67.4%	58.3%
Nume-Ref-II	0.68	1.07	65.5%	38.2%	10.7%	8.38	19.97	82.2%	65.7%	54.9%
Homo-Ref	0.61	1.05	68.5%	42.9%	14.9%	5.03	17.47	85.1%	74.5%	66.3%
PlaneFormers-TR [8], [25]	0.66	1.06	66.8%	37.5%	9.8%	8.96	20.01	83.0%	65.9%	53.5%
NOPE-SAC (ours)	0.52	0.94	73.2%	48.3%	16.2%	2.77	14.37	89.0%	86.9%	84.0%
ScanNet dataset										
Initial Pose	0.48	0.72	77.7%	51.9%	16.5%	14.68	26.75	73.7%	51.0%	34.4%
Nume-Ref-I	0.54	0.80	73.2%	47.2%	13.7%	16.57	29.47	68.7%	47.0%	32.3%
Nume-Ref-II	0.48	0.72	77.7%	51.8%	16.5%	14.64	26.72	73.7%	51.1%	34.6%
Homo-Ref	0.49	0.73	77.5%	51.3%	16.5%	14.03	26.27	74.2%	52.7%	36.8%
PlaneFormers-TR [8], [25]	0.48	0.72	78.3%	52.2%	14.2%	14.30	26.51	74.5%	52.2%	33.7%
NOPE-SAC (ours)	0.41	0.65	82.0%	59.1%	21.2%	8.27	22.12	82.6%	73.2%	59.5%

port3D [13] and the ScanNet [14] datasets. As it is shown, our method successfully reconstructs the scenes from sparse views even when the image overlap is very small (*e.g.*, the third row in Fig. 6) and the viewpoint change is very large (*e.g.*, the fourth row in Fig. 6).

5.7 Ablation for NOPE-SAC Pose Estimation

This section presents a series of ablation study for our NOPE-SAC pose estimation as it plays the most important

role for the end task. We use the initial pose achieved by our pose regression network by default.

NOPE-SAC VS. Other Pose Refinement Methods. Here, we first compare our NOPE-SAC with three traditional methods and one learning based method for pose refinement, including:

- (1) **Nume-Ref-I:** We use the numerical optimization like SparsePlanes [7] but only optimizes the initial camera



Fig. 6. Comparison of 3D plane reconstruction results on the Matterport3D [13] dataset (first four rows) and the ScanNet [14] dataset (last three rows). **Blue** and **Black** frustums show cameras of the first and the second images respectively.

poses $R^{(0)}, t^{(0)}$ as follows:

$$\min_{R,t} \sum_{\mathcal{P} \in \mathbb{P}} L(d_{\text{par}}(\mathcal{P}, R, t)) + d_{\text{pix}}(\mathcal{P}, R, t) + d_{\text{cam}}(R, R^{(0)}), \quad (21)$$

where \mathcal{P} is a pair of matched planes in the predicted plane correspondence set \mathbb{P} , $L(\cdot)$ is the Huber loss, d_{par} calculates the euclidean distance between plane parameters, d_{pix} is the reprojection error of matched SIFT [26] points on plane regions, and d_{cam} is a regularization term which restricts the geodesic distance of rotations.

- (2) **Nume-Ref-II**: A variant of Nume-Ref-I which excludes d_{pix} in Eq. 21.
- (3) **Homo-Ref**: We use homographies to estimate refined poses from predicted plane correspondences \mathbb{P} . Specifically, to each predicted plane correspondence $\mathcal{P} \in \mathbb{P}$, matched SIFT points are found from plane regions and then used to calculate the homography matrix H . Then a refined pose hypothesis can be decomposed from H . We use the scale of the initial translation and select

the refined pose from all hypotheses which minimizes $\sum_{\mathcal{P} \in \mathbb{P}} d_{\text{par}}(\mathcal{P}, R, t)$.

- (4) **PlaneFormers-TR** [8], [25]: We estimate the refined pose by giving planes detected by PlaneTR [25] and our regressed initial pose as inputs to the PlaneFormers [8].

As shown in Tab. 5, compared to the learning based PlaneFormers-TR [8], [25] which directly estimates a pose residual from features of all plane correspondences, our method improves the initial poses more effectively than PlaneFormers-TR [8], [25] on both two datasets with our accurate one-plane pose hypotheses. Benefiting from matched keypoints, the traditional Nume-Ref-I achieves the results which are most close to our NOPE-SAC on the Matterport3D [13] dataset. However, due to the difficulty to find sufficient good keypoint matches, Nume-Ref-I performs even worse than the initial pose on the ScanNet [14] dataset. Similarly, Homo-Ref also suffers from unsatisfied keypoint matches on the ScanNet dataset. In contrast, benefiting from directly learning pose refinement with plane parameters in embedding space, our NOPE-SAC avoids the problem of

TABLE 6

Ablation studies of the arbitrary initialization module and plane warping in NOPE-SAC pose estimation on the Matterport3D [13] and the ScanNet [14] datasets.

Settings		Trans.			Rot.		
AIM	Warp Plane	Med. ↓	Mean ↓	($\leq 0.5m$) ↑	Med. ↓	Mean ↓	($\leq 15^\circ$) ↑
Matterport3D dataset							
✓		0.61	1.00	42.3%	3.19	14.10	85.7%
	✓	0.51	0.92	49.3%	2.97	14.34	86.8%
✓	✓	0.52	0.94	48.3%	2.77	14.37	86.9%
ScanNet dataset							
✓		0.42	0.66	57.4%	8.17	22.05	73.2%
	✓	0.40	0.64	59.9%	8.21	21.95	73.0%
✓	✓	0.41	0.65	59.1%	8.27	22.12	73.2%

keypoints detection and matching and achieves state-of-the-art performance.

Arbitrary Initialization Module. In this part, we analyze the necessity of our arbitrary initialization module (AIM). As introduced in Sec. 4.1, the initial pose embeddings can be achieved from (1) the pose regression network or (2) the AIM. Thus, we first compare the influence of these two methods to pose refinement. As shown in Tab. 6, using initial pose embeddings from AIM achieves similar results to embeddings from the regression network, which demonstrates the effectiveness of our AIM. Furthermore, with the usage of AIM, our NOPE-SAC is flexible to refine initial poses that do not come from the convolutional pose regression network.

Plane Warping for Correspondence Embedding. Here, we discuss the influence of warping plane parameters before calculating correspondence embeddings as described in Eqn. 11. As shown in Tab. 6, warping plane parameters effectively improves the translation results, especially on the Matterport3D [13] dataset (*e.g.*, from 42.3% to 48.3%).

Pose Hypotheses Fusion. We then discuss the fusion strategies of one-plane pose hypotheses for pose refinement in Sec. 4.2, including (1)*Soft*, (2)*Avg*, (3)*Min-Cost*, (4)*Max-Score*. As shown in Tab. 7, all strategies, even selecting only one pose hypothesis (*Min-Cost* and *Max-Score*), can improve the initial pose, which demonstrates the effectiveness and the reasonability of our one-plane RANSAC. Specifically, when evaluating translations, *Avg* performs closely to *Soft*, while *Min-Cost* and *Max-Score* degenerate significantly on both two datasets. It indicates that it is necessary to leverage more than one hypothesis to get better translation refinement results. When evaluating rotations, both *Min-Cost* and *Max-Score* perform closely to or slightly better than *Soft*, while *Avg* degenerates significantly. It indicates that rotations can be refined more easily than translations with one rotation hypothesis. However, because of the influence of matching outliers and the plane parameter errors, the strategies of *Avg*, *Min-Cost*, and *Max-Score* are not stable for camera pose estimation. By contrast, *Soft* achieves the best overall performance benefiting from the learned pose scores.

Influence of Plane Parameters. In this part, we study the influence of plane parameter accuracy on our NOPE-SAC pose estimation on the Matterport3D [13] and the ScanNet [14] datasets. The upper bound of our method is achieved by using ground truth plane correspondences and ground truth plane parameters in our pose refinement,

TABLE 7

Ablation studies of NOPE-SAC pose estimation with different one plane pose fusion strategies on the Matterport3D [13] and the ScanNet [14] datasets.

Method	Trans.			Rot.		
	Med. ↓	Mean ↓	($\leq 0.5m$) ↑	Med. ↓	Mean ↓	($\leq 15^\circ$) ↑
Matterport3D dataset						
Initial Pose	0.69	1.08	37.0%	11.16	21.49	60.5%
Avg	0.56	0.96	45.3%	5.03	17.21	77.1%
Min-Cost	0.56	1.00	45.4%	2.85	14.47	86.8%
Max-Score	0.59	1.03	43.1%	2.84	14.38	87.0%
Soft	0.52	0.94	48.3%	2.77	14.37	86.9%
ScanNet dataset						
Initial Pose	0.48	0.72	51.9%	14.68	26.75	51.0%
Avg	0.42	0.65	57.8%	10.28	23.33	63.2%
Min-Cost	0.46	0.73	53.6%	8.75	22.68	72.1%
Max-Score	0.46	0.72	53.0%	8.77	22.91	72.4%
Soft	0.41	0.65	59.1%	8.27	22.12	73.2%

TABLE 8

Influence of plane parameter accuracy to NOPE-SAC pose estimation on the Matterport3D [13] and the ScanNet [14] datasets.

Setting	Trans.			Rot.		
	Med. ↓	Mean ↓	($\leq 0.5m$) ↑	Med. ↓	Mean ↓	($\leq 15^\circ$) ↑
Matterport3D dataset						
Initial Pose	0.69	1.08	37.0%	11.16	21.49	60.5%
w/ GT	0.32	0.70	63.5%	0.34	3.85	96.2%
(0.1m, 5°)	0.39	0.76	58.6%	3.27	6.85	95.4%
(0.2m, 10°)	0.48	0.83	51.5%	6.75	10.76	83.6%
(0.3m, 15°)	0.56	0.89	45.3%	10.40	15.17	66.0%
ScanNet dataset						
Initial Pose	0.48	0.72	51.9%	14.68	26.75	51.0%
w/ GT	0.26	0.47	72.1%	3.48	8.42	90.7%
(0.1m, 5°)	0.29	0.49	70.4%	7.22	11.63	88.2%
(0.2m, 10°)	0.35	0.55	65.4%	11.95	16.35	65.4%
(0.3m, 15°)	0.40	0.60	59.9%	16.35	21.11	44.3%

TABLE 9

Influence of the plane matching precision (P) to NOPE-SAC pose estimation on the Matterport3D [13] and the ScanNet [14] datasets.

Threshold	P	Translation			Rotation		
		Med. ↓	Mean ↓	($\leq 0.5m$) ↑	Med. ↓	Mean ↓	($\leq 15^\circ$) ↑
Matterport3D dataset							
0.2	49.9	0.52	0.94	48.3%	2.77	14.37	86.9%
0.1	48.8	0.52	0.94	48.4%	2.75	14.40	86.9%
0.01	46.4	0.53	0.94	47.9%	2.76	14.63	86.7%
0.001	44.7	0.53	0.94	47.7%	2.77	14.96	86.3%
ScanNet dataset							
0.2	44.3	0.41	0.66	59.1%	8.27	22.12	73.2%
0.1	43.0	0.41	0.65	58.9%	8.26	22.11	73.5%
0.01	40.8	0.41	0.65	58.6%	8.21	22.36	73.2%
0.001	39.8	0.41	0.65	58.5%	8.22	22.56	73.2%

defined as ‘w/ GT’ in Tab. 8. Then, we add various Gaussian noises to the offset and normal of ground truth plane parameters in both two image views. The mean of the Gaussian noises is set to zero. The standard deviation of plane offset increases from 0.1m to 0.3m, and the standard deviation of plane normal increases from 5° to 15°. As shown in Tab. 8, our method effectively improves the initial pose even in the challenging setting of (0.2m, 10°), but fails to improve rotations in the setting of (0.3m, 15°) on the ScanNet dataset because of too large noises on plane parameters. It demonstrates that our method is robust to the accuracy of plane parameters.

Influence of Matching Precision. Besides plane parameters, we also evaluate the influence of plane matching precision to our NOPE-SAC on the Matterport3D [13] and ScanNet [14] datasets. Here, a predicted plane correspondence is regarded as a true positive if it can be matched to a ground truth plane correspondence with mask IoU ≥ 0.5 in both two images. We conduct the experiments by gradually reducing the threshold of plane matching from 0.2 to 0.001. As shown in Tab. 9, with the reduction of the matching threshold, the plane matching precision reduces from 49.9 to 44.7 while the pose metrics only change slightly on the Matterport3D dataset. Similar results can be found on the ScanNet dataset. It demonstrates that our NOPE-SAC is able to cope with incorrect plane correspondences.

6 CONCLUSION

This paper studies the challenging two-view 3D reconstruction in a rigorous sparse-view configuration. At the core of estimating the camera poses from one-plane pose hypotheses generated from plane correspondences with neural networks, our proposed NOPE-SAC formulates the problem in a consensus sampling paradigm while enjoying end-to-end learning without incurring any offline optimization schemes. In the experiments, our NOPE-SAC achieves new state-of-the-art performances for sparse-view camera pose estimation and planar 3D reconstruction in indoor scenes on the challenging Matterport3D [13] and ScanNet [14] datasets. The comprehensive analyzes also align benchmarking protocols for sparse-view 3D reconstruction.

REFERENCES

- [1] A. Hartley and A. Zisserman, *Multiple View Geometry in Computer Vision* (2. ed.). Cambridge University Press, 2006. 1
- [2] D. J. Crandall, A. Owens, N. Snavely, and D. P. Huttenlocher, "Sfm with mrfs: Discrete-continuous optimization for large-scale structure from motion," *IEEE Trans. Pattern Anal. Mach. Intell.*, vol. 35, no. 12, pp. 2841–2853, 2013. 1
- [3] A. J. Davison, I. D. Reid, N. Molton, and O. Stasse, "Monoslam: Real-time single camera SLAM," *IEEE Trans. Pattern Anal. Mach. Intell.*, vol. 29, no. 6, pp. 1052–1067, 2007. 1
- [4] R. Mur-Artal, J. M. M. Montiel, and J. D. Tardós, "ORB-SLAM: A versatile and accurate monocular SLAM system," *IEEE Trans. Robotics*, vol. 31, no. 5, 2015. 1
- [5] J. L. Schönberger and J. Frahm, "Structure-from-motion revisited," in *IEEE Conf. Comput. Vis. Pattern Recog.*, 2016, pp. 4104–4113. 1
- [6] S. Qian, L. Jin, and D. F. Fouhey, "Associative3d: Volumetric reconstruction from sparse views," in *Eur. Conf. Comput. Vis.*, vol. 12360, 2020, pp. 140–157. 1, 3
- [7] L. Jin, S. Qian, A. Owens, and D. F. Fouhey, "Planar surface reconstruction from sparse views," in *IEEE Int. Conf. Comput. Vis.*, 2021. 1, 2, 3, 4, 6, 7, 8, 9, 10
- [8] S. Agarwala, L. Jin, C. Rockwell, and D. F. Fouhey, "Planeformers: From sparse view planes to 3d reconstruction," in *Eur. Conf. Comput. Vis.*, vol. 13663, 2022, pp. 192–209. 1, 2, 3, 7, 8, 9, 10, 11
- [9] P. Sarlin, D. DeTone, T. Malisiewicz, and A. Rabinovich, "Super-glue: Learning feature matching with graph neural networks," in *IEEE Conf. Comput. Vis. Pattern Recog.*, 2020, pp. 4937–4946. 1, 2, 3, 8, 10
- [10] D. Nistér, "An efficient solution to the five-point relative pose problem," *IEEE Trans. Pattern Anal. Mach. Intell.*, vol. 26, no. 6, pp. 756–777, 2004. 1, 3, 8
- [11] M. A. Fischler and R. C. Bolles, "Random sample consensus: A paradigm for model fitting with applications to image analysis and automated cartography," *Commun. ACM*, vol. 24, no. 6, pp. 381–395, 1981. 2, 3, 8
- [12] C. Raposo, M. Lourenço, M. Antunes, and J. P. Barreto, "Plane-based odometry using an RGB-D camera," in *Brit. Mach. Vis. Conf.*, 2013. 2
- [13] A. X. Chang, A. Dai, T. A. Funkhouser, M. Halber, M. Nießner, M. Savva, S. Song, A. Zeng, and Y. Zhang, "Matterport3d: Learning from RGB-D data in indoor environments," in *Int. Conf. 3D Vis.*, 2017, pp. 667–676. 2, 6, 7, 8, 9, 10, 11, 12, 13
- [14] A. Dai, A. X. Chang, M. Savva, M. Halber, T. A. Funkhouser, and M. Nießner, "Scannet: Richly-annotated 3d reconstructions of indoor scenes," in *IEEE Conf. Comput. Vis. Pattern Recog.*, 2017, pp. 2432–2443. 2, 6, 7, 8, 9, 10, 11, 12, 13
- [15] C. Godard, O. M. Aodha, M. Firman, and G. J. Brostow, "Digging into self-supervised monocular depth estimation," in *IEEE Int. Conf. Comput. Vis.*, 2019, pp. 3827–3837. 2
- [16] K. Lasinger, R. Ranftl, K. Schindler, and V. Koltun, "Towards robust monocular depth estimation: Mixing datasets for zero-shot cross-dataset transfer," *IEEE Trans. Pattern Anal. Mach. Intell.*, 2019. 2
- [17] T. Chen, S. An, Y. Zhang, C. Ma, H. Wang, X. Guo, and W. Zheng, "Improving monocular depth estimation by leveraging structural awareness and complementary datasets," in *Eur. Conf. Comput. Vis.*, vol. 12359, 2020, pp. 90–108. 2
- [18] W. Yin, Y. Liu, C. Shen, and Y. Yan, "Enforcing geometric constraints of virtual normal for depth prediction," in *IEEE Int. Conf. Comput. Vis.*, 2019, pp. 5683–5692. 2
- [19] Z. Li and N. Snavely, "Megadepth: Learning single-view depth prediction from internet photos," in *IEEE Conf. Comput. Vis. Pattern Recog.*, 2018, pp. 2041–2050. 2
- [20] A. Eftekhar, A. Sax, J. Malik, and A. Zamir, "Omnidata: A scalable pipeline for making multi-task mid-level vision datasets from 3d scans," in *IEEE Int. Conf. Comput. Vis.*, 2021, pp. 10766–10776. 2
- [21] R. Ranftl, K. Lasinger, D. Hafner, K. Schindler, and V. Koltun, "Towards robust monocular depth estimation: Mixing datasets for zero-shot cross-dataset transfer," *IEEE Trans. Pattern Anal. Mach. Intell.*, vol. 44, no. 3, pp. 1623–1637, 2022. 2
- [22] Z. Yu, J. Zheng, D. Lian, Z. Zhou, and S. Gao, "Single-image piecewise planar 3d reconstruction via associative embedding," in *IEEE Conf. Comput. Vis. Pattern Recog.*, 2019, pp. 1029–1037. 3
- [23] C. Liu, K. Kim, J. Gu, Y. Furukawa, and J. Kautz, "PlanerCNN: 3d plane detection and reconstruction from a single image," in *IEEE Conf. Comput. Vis. Pattern Recog.*, 2019, pp. 4450–4459. 3, 6
- [24] C. Liu, J. Yang, D. Ceylan, E. Yumer, and Y. Furukawa, "Planenet: Piece-wise planar reconstruction from a single RGB image," in *IEEE Conf. Comput. Vis. Pattern Recog.*, 2018. 3
- [25] B. Tan, N. Xue, S. Bai, T. Wu, and G. Xia, "Planetr: Structure-guided transformers for 3d plane recovery," in *IEEE Int. Conf. Comput. Vis.*, 2021, pp. 4166–4175. 3, 8, 9, 10, 11
- [26] D. G. Lowe, "Distinctive image features from scale-invariant keypoints," *Int. J. Comput. Vis.*, vol. 60, no. 2, pp. 91–110, 2004. 3, 8, 11
- [27] E. Rublee, V. Rabaud, K. Konolige, and G. R. Bradski, "ORB: an efficient alternative to SIFT or SURF," in *IEEE Int. Conf. Comput. Vis.*, 2011, pp. 2564–2571. 3
- [28] H. Bay, A. Ess, T. Tuytelaars, and L. V. Gool, "Speeded-up robust features (SURF)," *Comput. Vis. Image Underst.*, vol. 110, no. 3, pp. 346–359, 2008. 3
- [29] S. Leutenegger, M. Chli, and R. Siegwart, "BRISK: binary robust invariant scalable keypoints," in *IEEE Int. Conf. Comput. Vis.*, 2011, pp. 2548–2555. 3
- [30] J. Morel and G. Yu, "ASIFT: A new framework for fully affine invariant image comparison," *SIAM J. Imaging Sci.*, vol. 2, no. 2, pp. 438–469, 2009. 3
- [31] J. Revaud, C. R. de Souza, M. Humenberger, and P. Weinzaepfel, "R2D2: reliable and repeatable detector and descriptor," in *Adv. Neural Inform. Process. Syst.*, 2019, pp. 12405–12415. 3
- [32] D. DeTone, T. Malisiewicz, and A. Rabinovich, "Superpoint: Self-supervised interest point detection and description," in *IEEE Conf. Comput. Vis. Pattern Recog. Worksh.*, 2018, pp. 224–236. 3
- [33] Z. Luo, T. Shen, L. Zhou, J. Zhang, Y. Yao, S. Li, T. Fang, and L. Quan, "Contextdesc: Local descriptor augmentation with cross-modality context," in *IEEE Conf. Comput. Vis. Pattern Recog.*, 2019, pp. 2527–2536. 3
- [34] P. Lindenberger, P. Sarlin, V. Larsson, and M. Pollefeys, "Pixel-perfect structure-from-motion with featuremetric refinement," in *IEEE Int. Conf. Comput. Vis.*, 2021, pp. 5967–5977. 3

- [35] W. Jiang, E. Trulls, J. Hosang, A. Tagliasacchi, and K. M. Yi, "COTR: correspondence transformer for matching across images," in *IEEE Int. Conf. Comput. Vis.*, 2021, pp. 6187–6197. 3
- [36] X. Wei, Y. Zhang, Z. Li, Y. Fu, and X. Xue, "Deepsfm: Structure from motion via deep bundle adjustment," in *Eur. Conf. Comput. Vis.*, vol. 12346, 2020, pp. 230–247. 3, 7
- [37] A. Kendall, M. Grimes, and R. Cipolla, "Posenet: A convolutional network for real-time 6-dof camera relocalization," in *IEEE Int. Conf. Comput. Vis.*, 2015, pp. 2938–2946. 3, 7
- [38] P. Ji, R. Li, B. Bhanu, and Y. Xu, "Monoindoor: Towards good practice of self-supervised monocular depth estimation for indoor environments," in *IEEE Int. Conf. Comput. Vis.*, 2021, pp. 12767–12776. 3
- [39] S. En, A. Lechervy, and F. Jurie, "Rpnet: An end-to-end network for relative camera pose estimation," in *Eur. Conf. Comput. Vis.*, vol. 11129, 2018, pp. 738–745. 3
- [40] K. He, X. Zhang, S. Ren, and J. Sun, "Deep residual learning for image recognition," in *IEEE Conf. Comput. Vis. Pattern Recog.*, 2016, pp. 770–778. 3, 4
- [41] F. Milletari, N. Navab, and S. Ahmadi, "V-net: Fully convolutional neural networks for volumetric medical image segmentation," in *Int. Conf. 3D Vis.*, 2016, pp. 565–571. 3
- [42] B. Cheng, A. G. Schwing, and A. Kirillov, "Per-pixel classification is not all you need for semantic segmentation," in *Adv. Neural Inform. Process. Syst.*, 2021, pp. 17 864–17 875. 3
- [43] R. Sinkhorn and P. Knopp, "Concerning nonnegative matrices and doubly stochastic matrices," *Pac. J. Math.*, vol. 21, no. 2, pp. 343–348, 1967. 4
- [44] G. Peyré and M. Cuturi, "Computational optimal transport," *Found. Trends Mach. Learn.*, vol. 11, no. 5-6, pp. 355–607, 2019. 4
- [45] Y. Wu, A. Kirillov, F. Massa, W.-Y. Lo, and R. Girshick, "Detectron2," <https://github.com/facebookresearch/detectron2>, 2019. 7
- [46] I. Loshchilov and F. Hutter, "Decoupled weight decay regularization," in *Int. Conf. Learn. Represent.*, 2019. 7